Check for updates

Advanced Materials

ADVANCED MATERIALS
www.advmat.de

RESEARCH ARTICLE

A Universal Quasi-Atom Interaction Model and Application in Designing Single-Atom Catalysts for Alkali–Metal Chalcogenide Batteries

Chenhui Wang[1] | Wei Lin[2] | Hui Hu[1] | Yan Li[1] | Feng Pan[2] | Chengxin Wang[1]

[1]State Key Laboratory of Optoelectronic Materials and Technologies, School of Materials Science and Engineering, Sun Yat-Sen University, Guangzhou, People's Republic of China | [2]School of Advanced Materials, Peking University, Shenzhen Graduate School, Shenzhen, People's Republic of China

Correspondence: Yan Li (liyan266@mail.sysu.edu.cn) | Chengxin Wang (wchengx@mail.sysu.edu.cn)

Received: 29 April 2026 | **Revised:** 8 July 2026 | **Accepted:** 21 July 2026

Keywords: alkali–metal chalcogenide batteries | machine learning | quasi-atom interaction model | single-atom catalyst | valence electron counts

ABSTRACT

A deep understanding of reactant adsorption behaviors is crucial for unraveling structure–activity relationships and identifying simple descriptors for the kinetics of multi-electron redox reactions, such as the sulfur redox process in Li–S batteries (LSBs). Recently, the "10-electron rule" for evaluating the adsorption strength of single atoms (E_{ads}) has been established for free-atom-like single-atom alloys (SAAs). However, our density-functional theory calculations show that this rule is unfeasible for single-atom catalysts (SACs) with metal centers covalently coordinated by nonmetal atoms. Herein, we proposed a new 18-electron rule for covalent SACs by establishing the quasi-atom interaction model (*Q*-AIM), which interprets the U-type behavior of E_{ads}(S) dominated by antibonding-orbital filling. Additional calculations demonstrate that E_{ads}(S) can serve as an efficient descriptor of the kinetics of sulfur redox involving multiatom polysulfides. Then, guided by the efficient predictor and *Q*-AIM, we employed machine learning to screen ~800,000 candidate SACs. Ultimately, we obtained over 400 and 8000 promising SACs for sulfur evolution and sulfur reduction, respectively. Furthermore, E_{ads}(S) can be extended to predict the catalytic performance of SACs in Li/Na/K-S/Se batteries. This work not only simplifies complex multi-electron processes to single-atom adsorption energy but also establishes a link between occupied electronic states and the catalytic performance of SACs.

1 | Introduction

Catalysis lies at the heart of modern energy technologies, enabling key reactions in fuel conversion, storage, and utilization [1–3]. The rapid development of two-dimensional (2D) materials and single-atom catalysts (SACs) has vastly expanded the catalytic design space, offering tunable electronic structures through coordination environment engineering [4–10]. However, even for a simple substrate like graphene, the number of feasible SACs configurations can reach tens or hundreds of thousands [11, 12]. Coupled with the high cost of computing resources for complex electrochemical reactions, especially in multi-step catalytic cycles, this diversity demands a simple yet effective descriptor capable of bridging atom-level properties and catalytic behavior across materials and reaction types.

The electronic structure of a catalyst is crucial to its performance, as it governs how the catalyst interacts with reactants, intermediates, and products [13–18]. Among the models related to the electronic structure, *d*-band center theory is the most

Chenhui Wang and Wei Lin contributed equally to this work.

All rights reserved, including rights for text and data mining and training of artificial intelligence technologies or similar technologies.
© 2026 Wiley-VCH GmbH

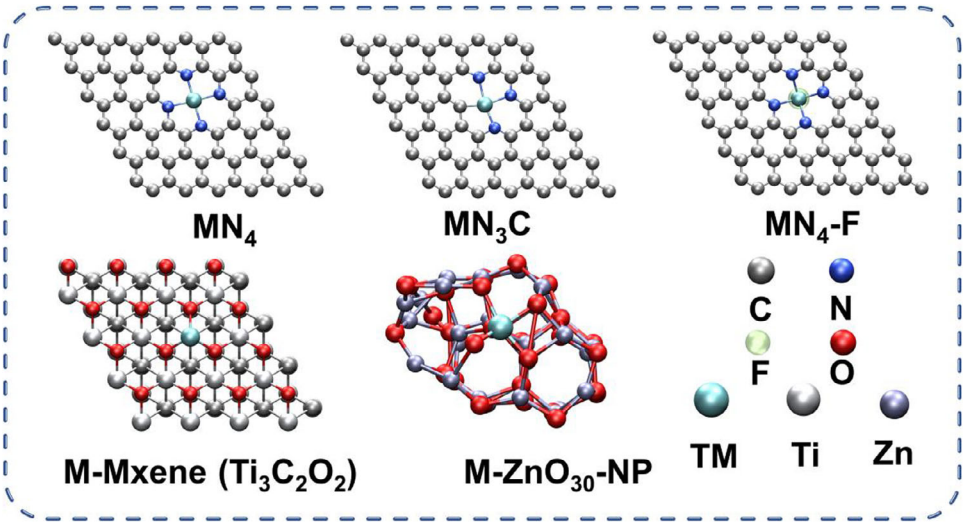


FIGURE 1 | Five types of covalent SACs with different coordination environments, including graphene- (MN_4/MN_3C/MN_4-F(axial-ligands-F)), MXene- ($Ti_3C_2O_2$), and ZnO_{30}-NP-based SACs [6]. TM refers to the active central transition metals.

widely utilized, which correlates the central position of the *d*-orbitals in the metal center with the strength of metal–adsorbate interactions [19–21]. While successful in describing simple systems, this model is limited when applied to complex, multi-electron catalytic processes. Specifically, it struggles to capture the full range of electronic interactions involved in reactions/adsorption [22]. In addition, one recent research [23] introduced a 10-electron rule to locate the minimum of single-atom (C/N/O/H) adsorption energy for single-atom alloy (SAA) catalysts, correlating adsorption strength and catalytic activity with the valence electron count of isolated metal sites. For a given adsorbate, accordingly, the transition-metal (TM) dopant with the strongest adsorption within a certain period can be determined. The decision is independent of the coordination environment of the active site, which yet constitutes a critical limitation when applied to SACs. Besides, this model remains confined to single-site and single-specie adsorption processes over free-atom-like centers [24], and cannot account for multi-site/multi-electron reactions. Furthermore, it struggles in cases where reactions require adsorption that is neither too strong nor too weak [25–27], as catalysts with intermediate adsorption strengths cannot be effectively distinguished. These issues greatly complicate the high-throughput screening of a huge number of candidate SACs.

Moreover, even if the fundamental principles of adsorption are well established, a significant gap remains between adsorption behavior and the resulting catalytic performance. This is particularly evident when describing the thermodynamic and kinetic aspects of multi-species chemical reactions. For example, the sulfur redox in Li–S battery (LSB) involves a 16-electron cascade, transforming elemental sulfur into various lithium polysulfides and ultimately into lithium sulfide (Li_2S) [28–30]. To accelerate sulfur redox, extensive research has been conducted to identify composite SACs with desired properties. However, two prohibitively expensive computations—the Li_2S decomposition energy barrier during oxidation and the free energy change of $Li_2S_2 \rightarrow Li_2S$ during reduction—have confined previous machine-learning-assisted high-throughput screening efforts to small datasets [31–34]. While several descriptors [35] have been proposed, such as the well-established Brønsted–Evans–Polanyi (BEP) [36–38] relations that simplify certain kinetic descriptions to sulfur electrochemistry, these approaches still require prohibitive computational resources given the vast configuration space of 2D SACs.

In this work, we proposed a novel quasi-atom interaction model (*Q*-AIM), which gives rise to an 18-electron count rule for predicting the binding trend of C/N/O/S atoms. Based on in-depth electronic property analysis, we innovatively correlate the simple adsorption energy of a sulfur atom with the catalytic performance of SACs for sulfur redox. Combining the *Q*-AIM with the density-functional-theory-assisted machine learning method, we further propose a universally applicable framework and workflow to screen SACs for alkali–metal-chalcogen batteries out of ~800,000 SACs with diverse coordination environments to identify optimal SACs.

2 | Results and Discussion

2.1 | Atomic Adsorption Over Covalently Bonded SACs

According to the previously established 10-electron rule, the strongest adsorption energy (E_{ads}) for single C, N, and O atoms on a series of TM centers in SAAs occurs when the total number of valence electrons in the adsorbate–metal center equals ten [23]. In other words, the E_{ads} of C, N, and O, with effective valence electron counts of 2, 3, and 4, reach a minimum at specific 4*d* TM centers—Ru ($\theta_M = 8$), Tc ($\theta_M = 7$), and Mo ($\theta_M = 6$)—where θ_M denotes the valence electron count of the metal center. Although E_{ads}(S) was not evaluated in Ref. [23], it can be reasonably inferred that its minimum would also occur at Mo ($\theta_M = 6$), given the chemical similarity between S and O. However, this rule was proposed based on species adsorption behavior on a series of free-atom-like SAAs, which might be inadequate for more abundant catalysts with covalent bonding environment around active

15214095, 0, Downloaded from https://advanced.onlinelibrary.wiley.com/doi/10.1002/adma.74445 by Wei Lin - Zhongshan University , Wiley Online Library on [04/08/2026]. See the Terms and Conditions (https://onlinelibrary.wiley.com/terms-and-conditions) on Wiley Online Library for rules of use; OA articles are governed by the applicable Creative Commons License

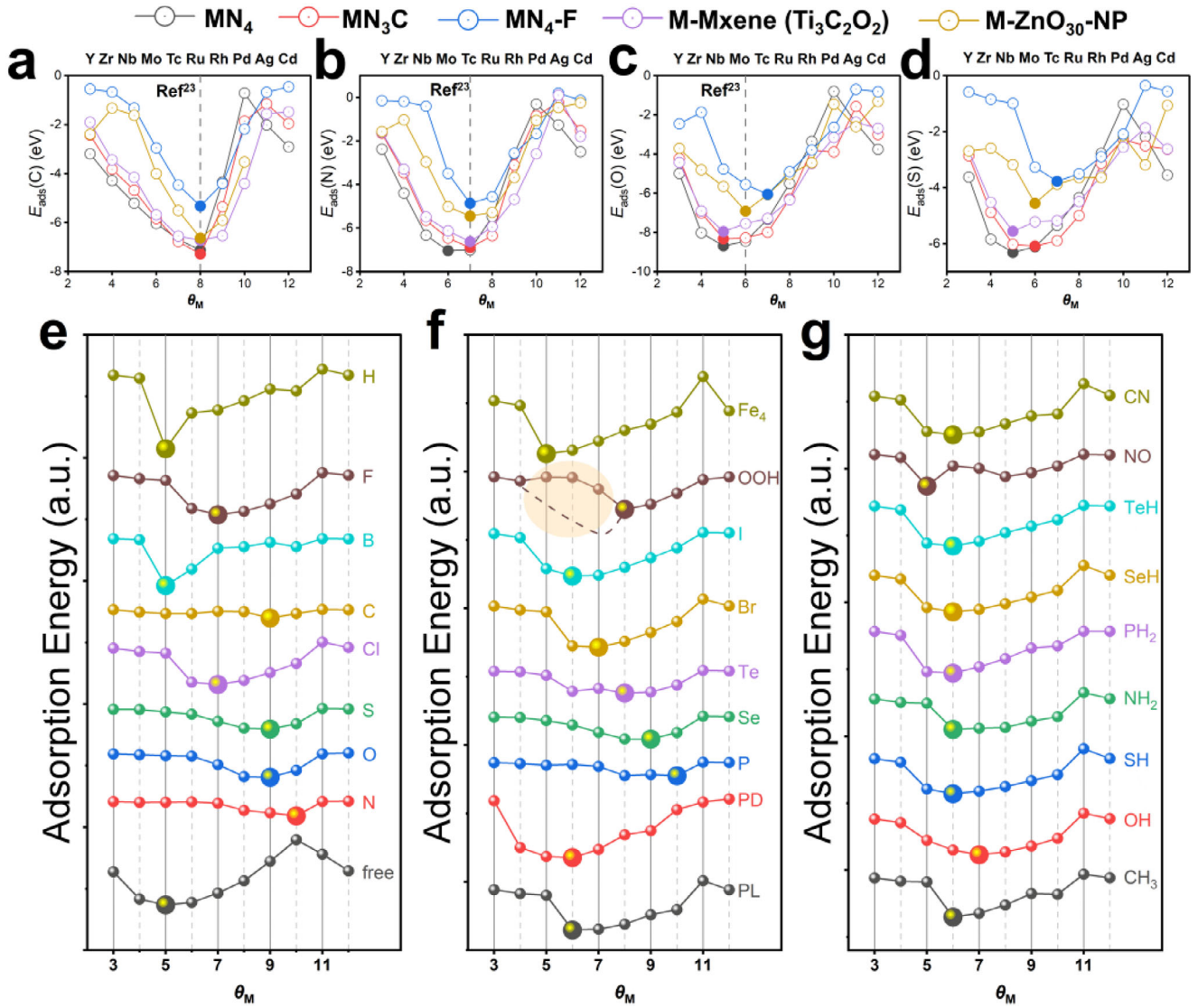


FIGURE 2 | The adsorption behavior of C/N/O/S atoms over covalent SACs. (a–d) The variation of adsorption energies of C (a), N (b), O (c), and S (d) atoms with respect to valence electron counts (θ_M) of 4*d* TMs centers supported by graphene (MN_4, MN_3C, MN_4-F), MXene ($Ti_3C_2O_2$), and ZnO_{30}-NP. The minimum E_{ads} values for different covalent SACs are marked by solid circles, while the gray dotted line indicates the minimum according to the "10-electron rule" [23] for SAAs. (e–g) The adsorption energy of S atom on 4*d*- MN_4 modified by varies axial ligands (AL) SACs, including H, F, B, C, O, N, I, Br, Te, Se, P, Cl, S, pyrrolic-N (PL), pyridinic-N (PD), Fe_4 cluster, CN, NO, CH_3, OH, SH, SeH, TeH, OOH, NH_2, and PH_2 species. θ_M refers to the outer electron number of the transition metal in periodic table.

centers. Therefore, we considered a series of covalent SACs, involving atomically dispersed TM centers supported by graphene, MXene, and metal-oxide nanoparticles (ZnO_{30}-NP) [6], as shown in Figure 1. This enables a systematic evaluation of whether the 10-electron rule remains valid in covalent SAC systems and how the coordination environment influences adsorption behavior.

To this end, we investigated the adsorption energies (E_{ads}) of C, N, O, and S atoms on 4*d* TMs supported by various substrates, including graphene-based systems (MN_4, MN_3C, and MN_4-F (F refers to a single fluorine atom serving as axil ligand)) as well as MXene and ZnO_{30}-NP. The adsorption energy minima for C and N are largely independent of the coordination environment of the metal centers (Figure 2a,b). In contrast, clear deviations are observed for O and S. As shown in Figure 2c, the minimum points for O adsorption are predominantly located at $\theta_M = 5$ (MN_4, MN_3C, MoS_2, and MXene) and $\theta_M = 7$ (MN_4-F), rather than $\theta_M = 6$ predicted by the 10-electron rule.

Similarly, for S adsorption (Figure 2d), the minima are widely distributed across θ_M values of 5–7 ($\theta_M = 5$: MN_4, MXene, MoS_2; $\theta_M = 6$: MN_3C, ZnO_{30}-NP; $\theta_M = 7$: MN_4-F). A broader distribution of E_{ads}(S) minima with respect to θ_M is observed for MN_4-type SACs modified with 26 axial ligands (AL) (Figure 2e–g). The configurations of these MN_4-AL SACs are available in Figure S1. As shown in Figure 2e,f, for SACs tailored by single-atom (SA) of H, F, B, C, O, N, I, Br, Te, Se, P, Cl, and S, the U-type E_{ads}(S) curves possess various bottom sites spanning θ_M = 5–10, markedly different from MN_4 SACs tailored by multi-atom functional group molecule, such as pyrrolic-N (PL), pyridinic-N (PD), Fe_4 cluster, CN, NO, CH_3, OH, SH, SeH, TeH, OOH,

15214095, 0, Downloaded from https://advanced.onlinelibrary.wiley.com/doi/10.1002/adma.74445 by Wei Lin - Zhongshan University , Wiley Online Library on [04/08/2026]. See the Terms and Conditions (https://onlinelibrary.wiley.com/terms-and-conditions) on Wiley Online Library for rules of use; OA articles are governed by the applicable Creative Commons License

NH_2, and PH_2 species, giving rise to the bottom sites locating around $\theta_M = 6$ as shown in Figure 2f,g. It should be noted that the brown area implies that E_{ads}(S) on MN_4-OOH SACs (M = Nb, Mo, and Tc) does not follow a U-type curve, owing to the disassociated *OOH adsorption type (see details in Note S1). In general, the bottom sites of E_{ads}(S) curves for 4*d* TMs are highly dependent with the coordination environments, which cannot be adequately explained by the 10-electron rule [23]. The discrepancy underscores the need for a more refined descriptive framework predicting the E_{ads}(S) minimum.

2.2 | Mechanisms of S–M Interaction Determining E_{ads}(S)

We next explored the orbital hybridization between S and MN_4 based on previously proposed molecular orbital (MO) theory [14, 23, 39]. In the typical S–MN_4 configuration, the active site adopts a five-coordinated geometry consisting of four in-plane nitrogen ligands and one top-adsorbed S atom. As illustrated in Figure 3a, this coordination environment gives rise to well-defined orbital interactions between the S *s*/*p* orbitals and the TM *s*/*d* orbitals. Specifically, σ bonding mainly originates from the interaction between S s/p_z and TM s/d_{z^2} orbitals, forming low-energy bonding states ($(s–s)\sigma$ and $(s–d_{z^2})\sigma$) and corresponding high-energy antibonding states ($(s–s)\sigma^*$ and $(p_z–d_{z^2})\sigma^*$). In parallel, π interactions arise from the coupling of S p_x/p_y with TM d_{xz}/d_{yz} orbitals, generating π and π^* states.

In contrast, the TM $d_{x^2-y^2}$ and d_{xy} orbitals exhibit minimal overlap with S orbitals due to symmetry mismatch and thus remain largely nonbonding (n_δ). In addition, partial hybridization between σ-type orbitals of $(s - d_{Z^2})\sigma^*$ and $(p_z–d_{z^2})\sigma$ leads to the formation of intermediate n_σ/σ states and σ^* states, reflecting orbital redistribution and weak bonding characteristics as described by the green lines in Figure 3a. Such orbital reconstruction can be identified by resolving orbital-resolved interactions across different energy windows using PDOS and COHP analyses. Overall, the interaction strength is determined by the competition among these states: bonding states (σ, π) stabilize the system, antibonding states (σ^*, π^*) weaken the interaction, and nonbonding states (n_σ/n_δ) contribute marginally.

The above qualitative analysis of orbital-wise interactions of the S and TM center in MN_4 SACs can be further confirmed by the projected density of states (PDOS) and crystal orbital Hamilton populations (COHP) analyses (see more details in Note S2). Two representative systems of ZrN_4 and TcN_4 were selected, locating on opposite sides of the bottom of the U-type adsorption energy curve (Figures 3b,c and S2), which enables us to investigate what exactly happens to orbital hybridization and orbital filling before and after the E_{ads}(S) passes through its minimum. As shown in Figure 3b, in ZrN_4, all the occupied states below the Fermi-energy (E_f) level are bonding states, of which the characteristics could be clearly distinguished by the inset partial-charge density. The peak near −10 eV arises primarily from 3*s*-5*s*/3*s*-$4d_{z^2}$ interactions corresponding to σ bonding characteristics. Near E_f, strong σ bonding ($3p_z$-$4d_{z^2}$) and π bonding ($3p_x$-$4d_{xz}$/$3p_y$-$4d_{yz}$) interactions are observed. Notably, the red curve in PDOS corresponds to nonbonding state (n_δ) orbitals ($d_{x^2-y^2}$/ d_{xy}).

In TcN_4, more significant occupation of antibonding states (σ^*/π^*) emerges, although the overall interaction characteristics remain like ZrN_4 (see Figure 3c). More interestingly, in the regions from −5 to −3 eV for ($3p_z$-$4d_{z^2}$) σ, hybridized 3*s*-$4d_{z^2}$ orbitals with σ^* character exist, resulting in new orbital redistribution between σ and σ^* (Figures 3c and S2). As shown in the lower right corner of Figure 3a, these two σ/σ^* states are partially cancelled out and split into σ^* state and σ/n_σ state. The corresponding σ^* orbitals are redistributed to higher energy levels. This orbital picture also provides a mechanistic basis for the deviation from the "10-electron rule" in covalent SACs, as the redistribution and occupation of σ and nonbonding states offers additional weaken/strengthen effect to stability, which thus can shift the optimal electron count away from the ideal value determined by the rule based on SAAs without redistribution procedure.

The above analysis indicates that the change of E_{ads}(S) on 4*d* MN_4 before and after crossing the minimum point NbN_4—specifically from ZrN_4 to TcN_4—is clearly marked by the occupation of antibonding states of ($3p_z$-$4d_{z^2}$) σ^*, ($3p_x$-$4d_{xz}$) π^* and ($3p_y$-$4d_{yz}$) π^*. This inspired us to investigate the variations of the charges from such occupied antibonding states ($Q_{anti\text{-}bonding}$) as well as that from bonding σ states of 3*s*-5*s*, 3*s*-$4d_{z^2}$, and $3p_z$-$4d_{z^2}$ and bonding π states from $3p_x$-$4d_{xz}$ and $3p_y$-$4d_{yz}$ ($Q_{bonding}$), aiming to explore the origin of the U-type trend of E_{ads}(S). As shown in Figure 3d, for 4d TMs before Mo, the growing occupation of bonding orbitals strengthens adsorption, leading to a gradual decrease in E_{ads}(S). For elements after Mo, however, the progressive filling of antibonding orbitals destabilizes the system, resulting in higher E_{ads}(S). Therefore, the S–M interaction is synergistically determined by the occupation of bonding/antibonding states, as quantified by the effective electron population: $Q_{eff} = Q_{bonding} - Q_{anti\text{-}bonding}$. We believe that a similar conclusion also holds for more SACs with more complicated coordination environments, given the U-type curve of $E_{ads}(S) \sim \theta_M$.

Then, we investigate the origin of such a wide range of the bottom positions of those curves from the electronic properties of SACs its self. The metal atomic orbitals interacting with the S atom are the 5*s*, $4d_{z^2}$, $4d_{xz}$, and $4d_{yz}$, among which the dominant contribution comes from the 4*d* orbitals. This implies that the centers of these three 4*d* sub-orbitals (Figure S3a,b) may directly determine the strength of the S–M interaction. Figure 3e shows the variation of E_{ads}(S) with the average band center of $d_{Z^2} + d_{xz} + d_{yz}$ for MN_3X (X = N, C, O, P, S and B, M = 3*d*, 4*d* and 5*d* TMs). Interestingly, this curve also exhibits a U-shaped feature, with its minimum occurring at an average band center of zero, that is, near the Fermi level. This *d*-band center position is the most moderate, resulting in the strongest interaction between the metal and S atoms. Considering the U-shaped relationship between E_{ads}(S) and θ_M, we naturally obtain an approximately linear relationship between the average band center and θ_M (see Figure 3f).

Although the origins of the variation trend and minimum locations of E_{ads}(S) have been identified to be correlated with occupation of bonding/antibonding states and average band centers of three 4*d* sub-orbitals, respectively, a more straightforward and general rule describing such behavior and particularly the energy minima is highly required. Previous orbital analysis demonstrates that the strength of the S–M interaction depends

15214095, 0, Downloaded from https://advanced.onlinelibrary.wiley.com/doi/10.1002/adma.74445 by Wei Lin - Zhongshan University , Wiley Online Library on [04/08/2026]. See the Terms and Conditions (https://onlinelibrary.wiley.com/terms-and-conditions) on Wiley Online Library for rules of use; OA articles are governed by the applicable Creative Commons License

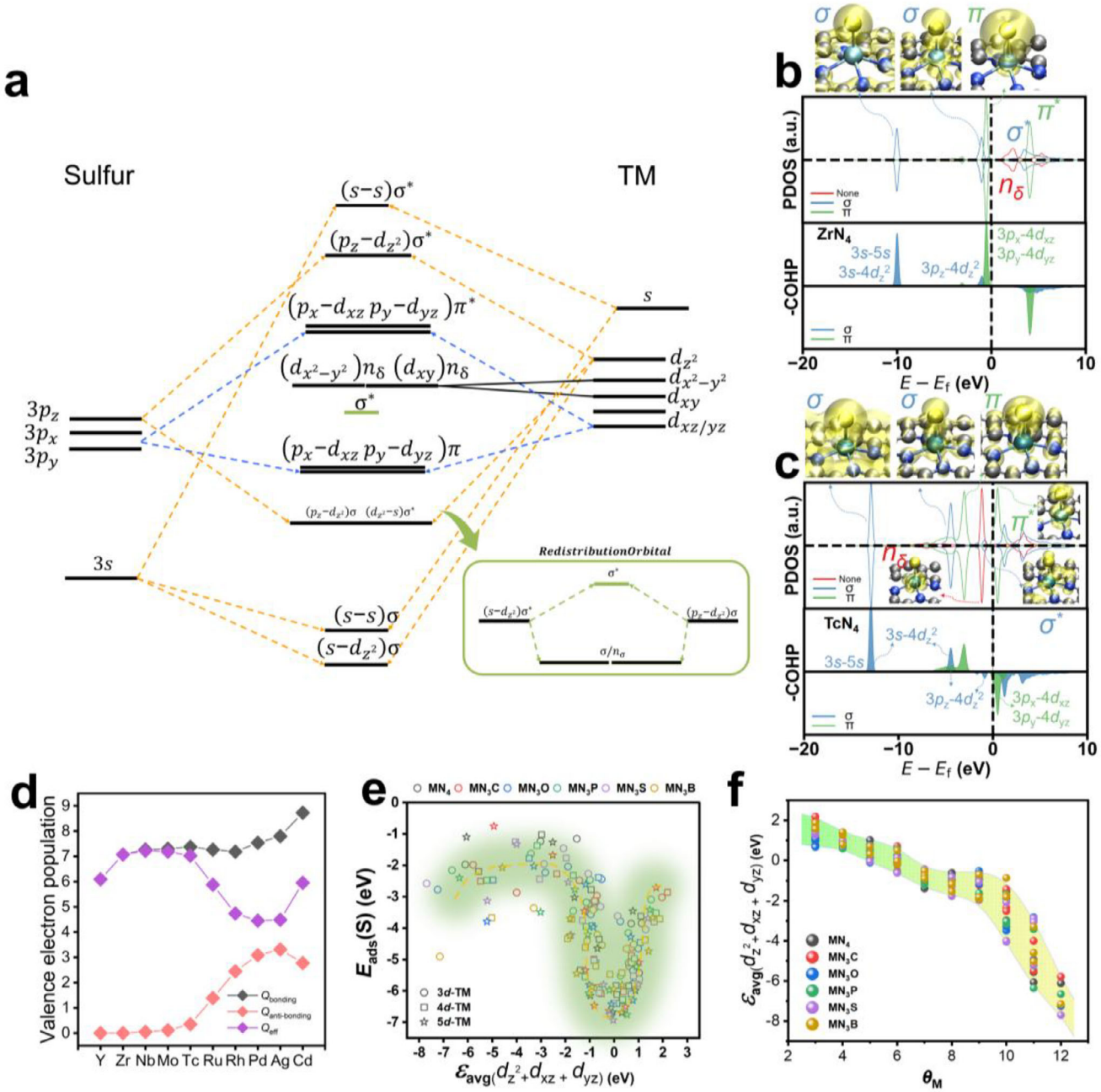


FIGURE 3 | Orbital-wise mechanistic analysis of S–M interactions. (a) The diagram of orbital-wise interactions between S and the active metal center atom, where σ, π, nonbonding, and redistribution relations are illustrated by orange, blue, black, and green dot line or area. (b, c) The orbital-wise projected density of states (PDOS) and crystal orbital Hamilton populations (COHP) analysis for ZrN_4 (b) and TcN_4 (c). The plots of the partial-charge density for occupied states are shown above the curves. For TcN4 (c), the partial-charge density of the occupied σ^*/π^* is also presented. (d) The orbital-wise electron population analysis of different interaction states for S adsorption over 4*d*-MN_4 SACs, where $Q_{eff} = Q_{bonding} - Q_{antibonding}$. (e) The reversed U-type rule for S adsorption energy by average *d*-orbitals center (ε_d) of $d_{z^2} + d_{xz} + d_{yz}$ orbitals of 3*d*, 4*d*, and 5*d* TMs dopants in MN_3X.(f) The correlation of average *d*-orbitals center (ε_d) of $d_{z^2} + d_{xz} + d_{yz}$ orbitals of 3*d*, 4*d*, and 5*d* TMs dopants varies with valence electrons number.

on the occupation of the hybridized *s*, *p*, and *d* orbitals from the adsorbate–metal–coordination (AMC) system. This motivates us to conceptualize the TM center and its ligands as an isolated quasi-atomic entity. Its most stable electronic configuration is a closed-shell $s^2p^6d^{10}$ state with 18 electrons (Figure 4a). Thus, we proposed a *Q*-AIM where an effective valence electron count (θ_{AMC}) of 18 indicates full occupation of orbitals and the lowest atomic energy in such a quasi-atom (Basic rules are available in Note S3 and Methods in Supporting Information). In other words, the strongest interaction of S–M occurs when $\theta_{AMC} \sim 18$. Considering different MN_3X SACs with diverse coordination environments, we found that the E_{ads}(S) minima were really given by those systems with θ_{AMC} of 16–18 (Figure 4b and Tables S1 and S2). Taking NbN_4 with the lowest E_{ads}(S) in MN_4 as an example, it has θ_{AMC} = 17 valence electrons: 2 × 4 from the four N atoms, 5 from Nb, and 4 from the adsorbed S atom (Figure S3c and Table S1). Additionally, we investigated the locations of adsorption energy minima for C/N/O/S atoms on

15214095, 0, Downloaded from https://advanced.onlinelibrary.wiley.com/doi/10.1002/adma.74445 by Wei Lin - Zhongshan University , Wiley Online Library on [04/08/2026]. See the Terms and Conditions (https://onlinelibrary.wiley.com/terms-and-conditions) on Wiley Online Library for rules of use; OA articles are governed by the applicable Creative Commons License

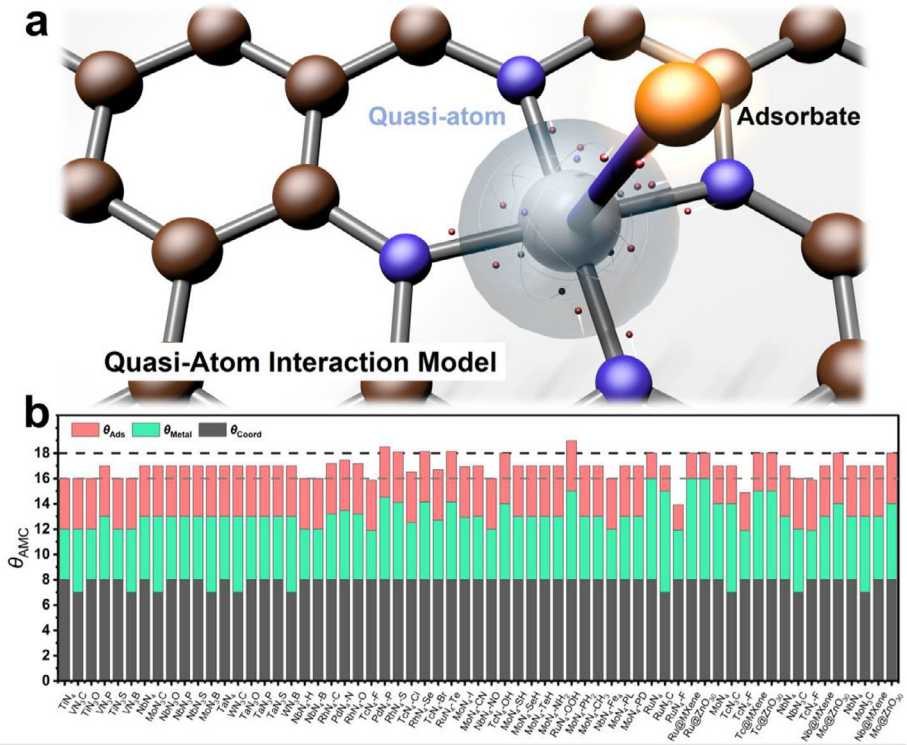


FIGURE 4 | Quasi-atom interaction model. (a) Schematic diagram of quasi-atom interaction model for adsorption on covalent substrate supported SACs. The gray ball denotes the quasi-atom, which has *s*,*p*,*d* electrons. (b) The counting results (θ_{AMC}) for SACs with relatively minimum in corresponding period- SACs, including electron count of adsorbate (θ_{Ads}), central metal (θ_{Metal}) coordination (θ_{Coord}).

various covalent substrates-supported SACs involved in Section 2.1 (Figure 4b and Tables S3 and S4). These locations of adsorption minima can be approved by *Q*-AIM with θ_{AMC} of 16–18. Note that among the SACs featuring 26 types of axil-ligands, those modified with three particular ligands require special attention—namely, OOH (ligand reconstruction on certain metal centers), Fe_4 clusters (electron delocalization), and F atom (strong charge localization due to its high electronegativity). Therefore, the actual electron counts for those three cases should be determined according to the relaxed local coordination environment, and more details can be found in Note S3 and Table S5.

In the subsequent machine-learning section, statistical analysis of the large dataset further supports the relevance of electron-count-related features in determining E_{ads}(S). It should be noted that the electron-count feature used in the machine-learning model is a nominal descriptor for data representation, whereas the corrected θ_{AMC} in *Q*-AIM is used for physical interpretation of local adsorption interactions.

Given the covalent nature of SACs, our new 18-electron rule based on *Q*-AIM significantly extends the previously proposed 10-electron rule [23] by explicitly accounting for the electronic states of both the metal center and its coordinated neighbors. This provides a universal physical framework for describing adsorbate–metal center interactions that covers both covalent SACs and free-atom-like SAAs, where orbital hybridization between the metal centers and their neighbors is weak.

Although the interaction mechanism between a single sulfur atom and metal centers in various SACs can be easily understood based on our newly proposed *Q*-AIM, a broader question remains: can such adsorption rules established for single atoms reliably predict the adsorption behavior of polyatomic molecules on metal centers—or even predict the catalytic performance of SACs for sulfur redox in LSB?

2.3 | Descriptor of E_{ads}(S) for Screening SACs for SER

The mechanism of charge–discharge process in LSB is displayed in Figure 5a, of which the efficiency is highly dependent on the kinetics of rate-determining step (RDS) of SER/SRR involving key intermediates of Li_2S/LiS [25, 32]. For SER, its kinetics is primarily governed by the energy barrier (E_b) for Li_2S cleavage. Due to the high computational cost of the NEB method, the BEP [38] relationship was usually adopted to calculate E_b, requiring the energy difference (ΔE) of initial-final states of Li_2S decomposition. As shown in Figure 5b, for each ΔE, several test calculations are essential for determining the energetically favored initial and final states of Li_2S decomposition. To identify the initial state, at least three types of Li_2S adsorption configurations are considered. For the final state, at least four configurations are tested to achieve Li—S bond breaking. However, when it turns to the vast configuration space, to screen SACs for SER using BEP relationship is still unfeasible.

We then explored the correlation of the adsorption behaviors of the S atom and adsorption and decomposition of Li_2S over MN_3X SACs (Figures 6 and S4). Upon being adsorbed on SACs, the Li_2S binds to the metal centers via the S atom. Therefore,

15214095, 0, Downloaded from https://advanced.onlinelibrary.wiley.com/doi/10.1002/adma.74445 by Wei Lin - Zhongshan University , Wiley Online Library on [04/08/2026]. See the Terms and Conditions (https://onlinelibrary.wiley.com/terms-and-conditions) on Wiley Online Library for rules of use; OA articles are governed by the applicable Creative Commons License

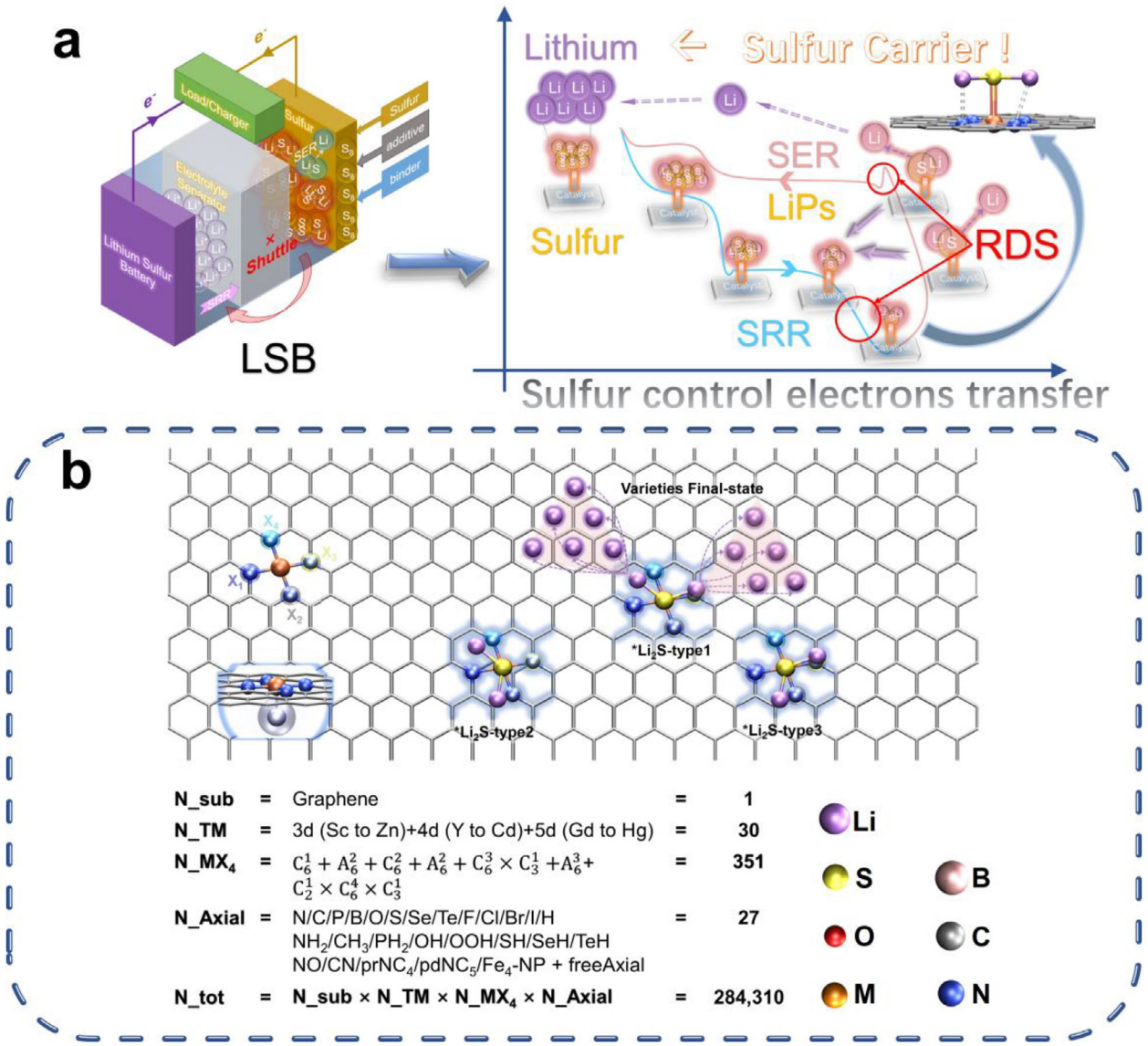


FIGURE 5 | (a) The schematic diagram of LSB and its redox process. (b) Coordination configuration diversity and reaction complexity of SER. Structure construction strategies of graphene-based MX_4 (X = N, C, O, P, S, and B) for possible configurations of Li_2S adsorption and decomposition. N_sub, N_TM, N_MX_4, and N_Axial refer to the number of substrate materials, doped transition metals, MX_4 4-coordination types, and axial ligands.

as shown in Figure 6a,b, similar U-type trends of adsorption energies for S and Li_2S can be obtained, implying that the S–M interaction predominantly governs the adsorption strength of Li_2S. This could be further confirmed by directly calculating the bonding strength based on ICOHP analysis on MoN_4, FeN_4, and CoN_4, as shown in Figure S4j,k. Taking the adsorption of Li_2S on MoN_4 as example, the S—Mo bond (ICOHP = −2.48) shows a significantly stronger bonding strength compared to Li—N (ICOHP > −1.64) and Li—S bonds (ICOHP = −0.58), indicating that the dominant electronic interaction occurs between the S atom and the metal center upon Li_2S being adsorbed. While for the adsorption behavior of LiS, it can be inferred to be similar with Li_2S, showing key interaction of S–M among multi-sites adsorptions.

As shown in Figures 6c and S5a, E_{ads}(S) varies linearly with integrated COHP (ICOHP) of Li—S bond in adsorbed Li_2S across each period of TMs, implying the positive correlation between adsorption strength of S atom and the degree of Li—S bond activation and even the kinetics of Li_2S decomposition. Therefore, we expect that E_{ads}(S) might be an efficient descriptor for predicting E_b of Li_2S decomposition. To valid this assumption, sufficient E_b data are required.

As shown in Figure 6d, for MN_3X (M = Ti, Fe, Co, Cu, Zn, Mo, Ta, and W; X = N, C, O, P, S, and B) SACs, the correlation between E_b and ΔE can be described by $E_b = 1.00\Delta E + 0.17$ eV. Using this BEP relationship, we calculated the ΔE values for additional MN_3X SACs and estimated their E_b values (Figure S5c–f), which also exhibit U-type correlations with θ_M for 3*d*/4*d*/5*d* TMs. Notably, metal centers of V, Nb, Mo, Ta, and W with N_3X coordination configurations possess superior SER catalytic performance, with E_b falling within 0.40–0.80 eV (details see Figure S5 and Note S4). These energy barriers exhibit strong dependence on the ICOHP of Li—S bond: higher ICOHP values correspond to lower E_b, indicating that greater Li—S bond activation facilitates Li_2S

15214095, 0, Downloaded from https://advanced.onlinelibrary.wiley.com/doi/10.1002/adma.74445 by Wei Lin - Zhongshan University , Wiley Online Library on [04/08/2026]. See the Terms and Conditions (https://onlinelibrary.wiley.com/terms-and-conditions) on Wiley Online Library for rules of use; OA articles are governed by the applicable Creative Commons License

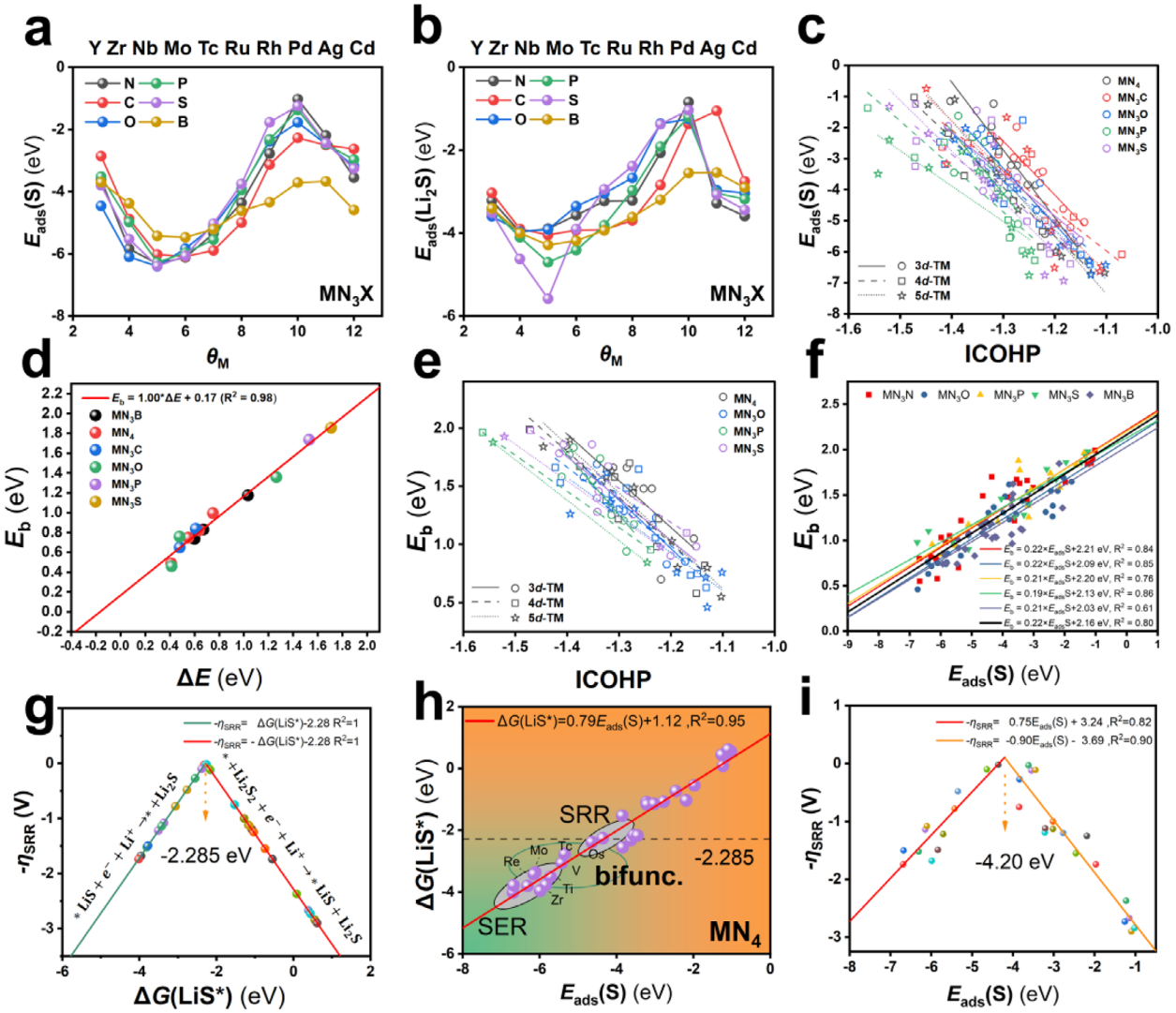


FIGURE 6 | The correlation of E_{ads}(S) and SER/SRR performance of MN$_3$X SACs. (a, b) Adsorption energies of S (a) and Li$_2$S (b) on MN$_3$X, where M is from 4*d* TMs. (c) The variation of E_{ads}(S) with ICOHP for *M*N$_3$X, *M* is from 3*d*, 4*d*, and 5*d* TMs. (d) The variation of E_b with Δ*E* for Li$_2$S decompositions over several MN$_3$X SACs. (e) The values of E_b as functions of ICOHP over a few MN$_3$X. (f) Linear correlation of E_{ads}(S) and E_b for MN$_3$X; the black bold line refers to the combined fitting result. E_b values are obtained by NEB method or BEP relationship. (g) The volcanic relation of negative value of overpotential ($-\eta_{SRR}$) of SRR with ΔG_{LiS*}. (h) The value of ΔG_{LiS*} linearly correlated with E_{ads}(S). The green circle refers to probable bifunctional catalysts for SER and SRR. (i) The volcanic relation of value of $-\eta_{SRR}$ with E_{ads}(S).

decomposition (Figures 6e and S5b). As anticipated, positive linear variations of E_b with E_{ads}(S) across MN$_3$X SACs (Figure 6f) confirm that the complex kinetics of Li$_2$S decomposition can be reliably predicted using only E_{ads}(S). This offers a significant computational advantage over the more computationally intensive approach based on the BEP relationship. The effective descriptor E_{ads}(S) enables rapid screening of potential SACs for Li—S decomposition.

2.4 | Descriptor of E_{ads}(S) for Screening SACs for SRR

For SRR proceeding through a sequential conversion pathway from cyclic S$_8$ to Li$_2$S, the Li$_2$S$_2$ → Li$_2$S conversion was adopted as a representative rate-determining solid–solid step (RDS) for evaluating the overpotential (η^{SRR}) [25, 31], following the commonly used electrocatalytic model for sulfur reduction (reaction mechanism see Method in Supporting Information). This treatment is also consistent with our full-pathway SRR free-energy calculations on representative SACs with different coordination environments (see Figure S6, Table S6, and Note S5). As shown in Figure 6g, these free energy changes have linear correlations with the adsorption free energy of LiS (ΔG_{LiS*}), with more details demonstrated in Note S5. Additional DFT calculations show that E_{ads}(LiS) and ΔG_{LiS*} varies linearly with E_{ads}(S) (Figures 6h and S7a) and thus E_{ads}(S) is accordingly confirmed to be an excellent descriptor for predicting optimal η_{SRR} via a volcanic relationship, with peak η_{SRR} locating at E_{ads}(S) = −4.20 eV (Figure 6i).

Our calculations identify E_{ads}(S) as an efficient descriptor for predicting the performance of SACs for both SER and SRR. To further confirm its uniqueness and superiority, we also evaluated other readily accessible properties, including Li adsorption energy,

15214095, 0, Downloaded from https://advanced.onlinelibrary.wiley.com/doi/10.1002/adma.74445 by Wei Lin - Zhongshan University , Wiley Online Library on [04/08/2026]. See the Terms and Conditions (https://onlinelibrary.wiley.com/terms-and-conditions) on Wiley Online Library for rules of use; OA articles are governed by the applicable Creative Commons License

d-band center, Bader charge, and the integrated crystal orbital Hamilton population (ICOHP) of the Li—S bond in adsorbed Li_2S. As shown in Figures S8 and S9; Note S5, $E_{ads}(S)$ is the only descriptor that simultaneously shows clear correlations with both E_b and η_{SRR}. Although the ICOHP for Li—S bond in $*Li_2S$ varies linearly with E_b, it mainly reflects Li—S bond activation during the Li_2S oxidation and does not provide a unified prediction of both SER and SRR performances. This conclusion is also supported by model-free statistical analyses using Kraskov–Stögbauer–Grassberger mutual information (KSG MI) [40, 41] and the Chatterjee correlation coefficient (ξ) [42], confirming that $E_{ads}(S)$ is statistically more suitable for describing sulfur redox activity than the competing descriptors.

We subsequently investigated MN_4-type SACs as promising bifunctional catalysts toward both SER and SRR. For MN_4 SAC candidates, WN_4 (E_b = 0.55 eV) and MoN_4 (E_b = 0.58 eV) show the best performance for SER, and VN_4, NbN_4, TaN_4, and ReN_4 also show competitive SER catalytic performance ($E_b \sim$ 0.80 eV). For SRR, ScN_4, YN_4, RuN_4, CdN_4, GdN_4, and OsN_4 exhibit promising performance with $\eta_{SRR} < 0.30$ V, and TcN_4, VN_4, and CrN_4 exhibit potential catalytic performance (η_{SRR} of 0.50–0.80 V). More details are available in Note S5 and Figure S7c. These results reveal a descriptor-defined balance between SER and SRR, because the two processes favor different ranges of S adsorption strength. For SER, stronger S adsorption promotes Li—S bond activation and lowers the Li_2S decomposition barrier. In contrast, SRR follows a volcano-type dependence on $E_{ads}(S)$, with the optimal value located near $E_{ads}(S) \approx -4.20$ eV. Therefore, an efficient bifunctional SAC should exhibit moderately strong S adsorption, slightly stronger than that corresponding to $E_{ads}(S)$ of −4.20 eV but not excessively strong. This descriptor-defined trade-off region is highlighted in Figure 6h.

To make this region more explicit, representative metal centers located in or near this region have been labeled in Figure 6h, and their DFT-derived performance metrics are summarized in Table S7. Among the MN_4 candidates, VN_4 shows the most balanced bifunctional behavior, with η_{SRR} = 0.78 V and E_b = 0.70 eV. TiN_4, VN_4, ZrN_4, MoN_4, TcN_4, ReN_4, and OsN_4 show nearly bifunctional activity, whereas their SER and/or SRR activity is relatively moderate. These results suggest that the present single-metal SAC space is subject to an intrinsic SER/SRR trade-off, and that further coordination or multi-site design may be required to achieve simultaneously optimized bifunctional sulfur redox catalysis.

Given the intrinsic trade-off within the conventional MN_4 configuration, it is imperative to explore SACs with diverse coordination environments and varying substrates. In addition to graphene, we also selected C_3N as a representative N-rich covalent 2D support, because it can stabilize MN_4-type single-atom sites with a local coordination motif comparable to graphene-supported MN_4 SACs while providing a distinct substrate electronic environment. This allows us to examine the transferability of $E_{ads}(S)$ and expand the descriptor-guided screening to a broader configuration space, as further supported by the consistent U-type adsorption trends and the $E_{ads}(S)$–$E_{ads}(Li_2S)$ scaling relationship shown in Figure S10 and Note S7.3. For configuration space of MX_4 SACs (X = N, C, O, P, S and B) supported by graphene (bottom in Figure 5b), there are C_6^1 for $M(X_1)_4$, A_6^2 for $M(X_1)_3X_2$, $C_6^2+A_6^2$ for $M(X_1)_2(X_2)_2$, $C_6^3\times C_3^1+A_6^3$ for $M(X_1)_2X_2X_3$, and $C_2^1\times C_6^4\times C_3^1$ for $MX_1X_2X_3X_4$ (X_{1-4} means distinct heteroatoms), yielding a total of 351 unique coordination types. Further considering the axial modulation with 26 additional ligands, we can obtain a total of 284,310 distinct SACs. Owing to the high symmetry of the graphene lattice, the configurations based on graphene are relatively conservative. When it turns to more complex substrates such as C_3N, the number of configurations nearly doubles due to their low symmetry (Figure S11). Compared with configurations of graphene-based SACs, only MX_4 and β-/γ- $M(X_1)_2(X_2)_2$ supported by C_3N do not have another mirror counterpart with a different configuration. The configurations for C_3N-based SACs can be as high as 539,460. Although our newly proposed descriptor of $E_{ads}(S)$ is more efficient than the other descriptors [25, 31, 32, 35], high-throughput calculations for screening SACs toward sulfur redox guided by $E_{ads}(S)$ is still unfeasible due to the vast configurational space of SACs supported by graphene and C_3N (~800,000 entries). Therefore, machine learning methods become the optimal choice for solving this issue.

2.5 | Screening SACs for LSB via $E_{ads}(S)$ Predicted by Machine Learning Guided by *Q*-AIM

With 15 input features targeting the output property $E_{ads}(S)$, a series of machine learning (ML) studies were conducted to screen high-performance SACs supported by graphene and C_3N for LSB (Tables S8 and S9). Initially, a DFT-based dataset of $E_{ads}(S)$ covering 1449 SACs was used to train 13 different ML models (Figure 7a). PCA analysis (see Figure S12a) confirms that the training dataset adequately covers the targeted chemical space and captures its principal distribution directions. Among the 15 features, the total electrons of the metal-centered entity of $\theta_T = \theta_M + \theta_C + \theta_A$ reflects the S–M interaction strength as interpreted by our newly proposed *Q*-AIM, where θ_M, θ_C, and θ_A are the effective electrons of metal centers, coordinated atoms, and AL, respectively. To further distinguish different coordination environments of SACs, we introduced the electronegativity-based descriptors: χ_Δ and χ_A, which help resolve structural ambiguities among similar configurations (details of descriptors construction are available in Note S6 and Figure S12b). Then the hyperparameter optimization for all ML models was carried out using a stepwise grid search approach (Figure S13b). Among 13 ML models, CatBoost [43] demonstrated the best predictive performance with R^2 of 0.99 (training), 0.96 (validation), and 0.93 (test) (Figures 7b–d), indicating strong generalization capability and superior accuracy in predicting $E_{ads}(S)$.

To elucidate the internal decision-making mechanism of the CatBoost model, four quantitative metrics were employed to assess the contribution of each feature to $E_{ads}(S)$. As demonstrated in Figure 7e and Note S6, the importance analyses reveal that the features of atom number of AL (n_A) and valence electron number of θ_T, θ_M, and θ_A exhibit the highest importance; especially n_A is the most critical intrinsic feature revealing the significant influence of ALs. By employing individual feature-level SHAP [44] analysis (Figure 7e, right), the feature-specific directional effects were further performed to evaluate the structure-performance correlation and confirm the robustness of *Q*-AIM, as shown

15214095, 0, Downloaded from https://advanced.onlinelibrary.wiley.com/doi/10.1002/adma.74445 by Wei Lin - Zhongshan University , Wiley Online Library on [04/08/2026]. See the Terms and Conditions (https://onlinelibrary.wiley.com/terms-and-conditions) on Wiley Online Library for rules of use; OA articles are governed by the applicable Creative Commons License

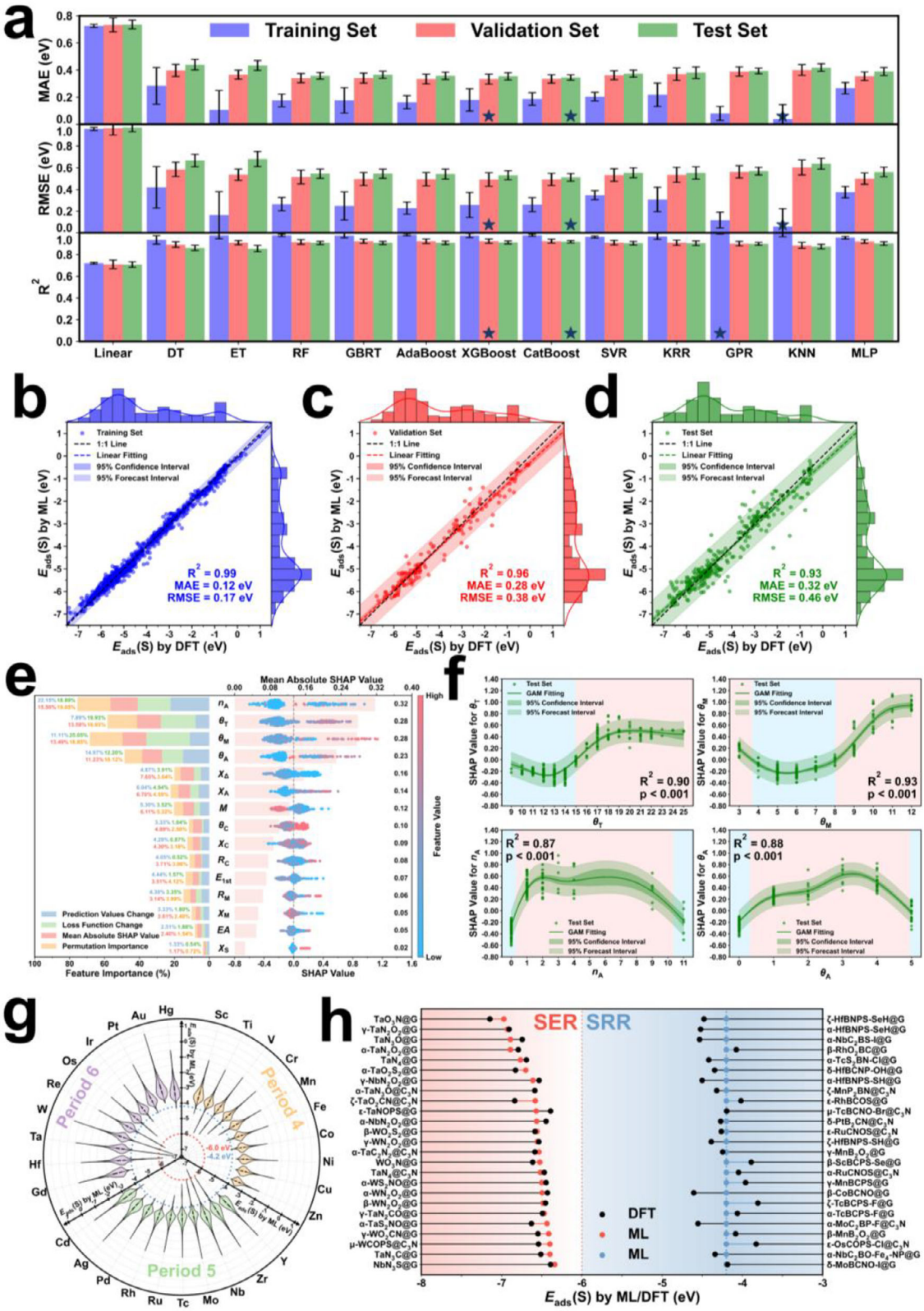


FIGURE 7 | E_{ads}(S) of 800,000 graphene- and C_3N-supported SACs predicted by ML. (a) Prediction accuracy (MAE, RMSE, and R^2) of 13 ML models. (b–d) Prediction results of the CatBoost model on the training (b), validation (c), and test (d) set. (e) Relative importance in the test set based on four methods and distribution of SHAP values for each feature. (f) SHAP value dependence plots for the four most important features (namely θ_T, θ_M, n_A, and θ_A) in the test set. (g) E_{ads}(S) of 823,770 SACs predicted by the CatBoost model. (h) Potential high-performance SACs for SRR/SER mined by ML and their DFT verification with average MAE values of 0.0.20/0.09.

15214095, 0, Downloaded from https://advanced.onlinelibrary.wiley.com/doi/10.1002/adma.74445 by Wei Lin - Zhongshan University , Wiley Online Library on [04/08/2026]. See the Terms and Conditions (https://onlinelibrary.wiley.com/terms-and-conditions) on Wiley Online Library for rules of use; OA articles are governed by the applicable Creative Commons License

in Figures 7f and S14. Specifically, the effect of θ_T for E_{ads}(S) shifts from negative to positive when it reaches ~15, and for the case $\theta_T > 18$, the effect shows strongly positive, indicating that the adsorption energy minimum occurs before $\theta_T = 15$ and the maximum occurs when $\theta_T > 18$. Given that the valence electron count of S is 4, it follows that E_{ads}(S) lies at its minimum when the total number of electrons is less than 4 + 15 = 19. This finding supports our proposed *Q*-AIM, which predicts the strongest interaction between S and the metal centers when the total number of electrons in the quasi-atom is around 18. Additionally, with the SHAP analysis of θ_M, n_A, and θ_A in Figure 7f, we can conclude that the E_{ads}(S) minimum distributes among TMs with θ_M of 4–8, and AL would weaken the adsorption strength of S as their markedly competition with S adsorbate.

We next predicted E_{ads}(S) of 823,770 SACs using ML guided by *Q*-AIM. As shown in Figure 7g, the performance distribution reveals that SACs with diverse TMs can meet the criteria for superior SRR catalysts (8977 promising SACs for SRR with E_{ads}(S) ≈ −4.2 eV). For example, SACs anchored with Nb, Mo, Tc, and Hf possess a considerable proportion of high-activity configurations, which exceed 2.5% of all available coordination geometries for each metal site (Table S10). However, high-performance SER catalysts are primarily restricted to specific elements (Nb, Mo, Hf, Ta, W, and Re). In total, we obtained 460 promising SACs for SER with E_{ads}(S) < −6.0 eV, yielding the lowest E_b ≈ 0.55 eV (Table S10), which reflects the optimal performance within the descriptor-guided chemical space of MX_4 supported on graphene/C_3N. Accordingly, potential SACs for SER are typically devoid of ALs and concentrated on several metal dopants, which further confirms our earlier conjectures and offers a new avenue for SACs designing. The predictions of ML were further validated by DFT calculations regarding 50 potentially efficient SACs for SER/SRR, as shown in Figure 7h.

Furthermore, the results of ML give rise to some key principles for designing such SACs (see details in Note S6). For example, (1) introduction of ALs is unfavorable for the decrease of E_{ads}(S) and accordingly the improvement of SER performance; (2) symmetry-breaking via heteroatom doping facilitates achieving lower E_{ads}(S) and enhancing the SER performance; (3) the incorporation of a large quantity of P and S (atoms with large radius) is unfavorable for lowering E_{ads}(S); (4) Heavier 5*d* TMs tend to weaken the S–M interaction more effectively than their 3*d* and 4*d* counterparts. To further examine the practical relevance of the descriptor-derived design principles, we compared our predictions with representative experimental Li—S studies (Note S6 and Table S11). The predicted Fe/Co/Ni activity trends, namely, FeN_4 ≈ CoN_4> NiN_4 for SER and FeN_4> CoN_4> NiN_4 for SRR, are broadly consistent with available CV-based and Li_2S-deposition experimental comparisons. Moreover, previous works about asymmetric Fe-, Co-, Ni-, and W-based catalysts provide additional support for the roles of coordination-symmetry breaking, heteroatom regulation, and heavy TM centers in tuning sulfur redox activity. These comparisons suggest that the *Q*-AIM/E_{ads}(S)-guided framework offers a reasonable active-site-level guideline for SAC design, although practical cell performance is also affected by electrode-level factors.

2.6 | Extended Application of E_{ads}(S) for Screening SACs in Alkali–Metal Chalcogenide Batteries

To assess the universality of the descriptor E_{ads}(S) and *Q*-AIM, we systematically evaluated its ability to predict the catalytic performance of SACs across different substrates and battery systems. We constructed SACs anchored on diverse 2D-substrates, including BN, MoS_2, LDH, Au (111), and $Ti_3C_2O_2$ MXene, as illustrated in Figure 8a. Note that two distinct coordination environments for SACs on BN (Figure S15a,b) were considered, corresponding to anchored sites of single vacancy (BN-SV) and double vacancy (BN-DV), respectively.

Similar U-type variations in adsorption energies for S, LiS, and Li_2S as a function of θ_M were consistently observed across the studied SAC platforms with different substrates (Figure 8b–d). The minima of E_{ads}(S) for the different SACs could still be estimated based on the *Q*-AIM-derived electron counting rule (Table S3). Accordingly, the lowest points of the U-type E_{ads}(S) curves occur at Nb for MXene, MoS_2, and BN-SV, and at Mo for LDH, Au (111), and BN-DV. A similar U-type trend was also evident for LiS adsorption, with minima located at Nb sites on MXene, MoS_2, Au (111), and BN-DV. For Li_2S adsorption, however, this rule applies only to SACs supported on MXene, MoS_2, and Au (111), with deviations observed on LDH and BN substrates (more discussions are available in Note S7 and Figure S15c). Notably, considering S adsorption over SAA (Mo@MoS_2 and Nb@Au111), in which the TM exhibits negligible covalency akin to a free atom, our *Q*-AIM is simplified as 10 electrons rule considering the d^{10} configuration of the quasi-atom entity, in agreement with previous work [23]. Generally speaking, the U-type adsorption behavior can be observed in various adsorbates and diverse catalysts (SACs with covalent environment and SAAs with free-atom-like centers), which can be supported by our *Q*-AIM and corresponded 18-electron rule.

Next, the correlation patterns between E_{ads}(Li_2S/LiS) and E_{ads}(S) were examined, as shown in Figure 8e,f. These positive linear correlations link S adsorption with LiS/Li_2S adsorption and even with η_{SRR}/E_b, indicating that E_{ads}(S) can predict effectively SRR/SER performance of SACs on substrates of MoS_2, Au(111), and MXene. Interestingly, as shown in Figure 8e, the slopes relating E_{ads}(S) to E_{ads}(Li_2S) vary considerably with substrates, suggesting that SER performance of SACs on such three substrates responds with different sensitivities to sulfur adsorption strength. In contrast, it is relatively uniform for SRR, with slope values ranging from 0.66 to 0.87 (Figure 8f).

The descriptor framework can also be extended to predict the reaction kinetics in alkali–metal (Li, Na, and K) -sulfur/selenium batteries. Inspired by previous results, we assumed that the catalytic performances of SACs for charge/discharge processes in both M–S and M–Se batteries can be strongly correlated with E_{ads}(S) and E_{ads}(Se). Moreover, given the chemical similarities between sulfur and selenium, E_{ads} (S) might serve as a universal descriptor. Taking the sulfur/selenium oxidation during the charge process as an example, we found that the E_b values for Na_2S and Li_2Se decompositions (obtained via NEB method and BEP relationship shown in Figure S15d) vary with θ_M, exhibiting

15214095, 0, Downloaded from https://advanced.onlinelibrary.wiley.com/doi/10.1002/adma.74445 by Wei Lin - Zhongshan University , Wiley Online Library on [04/08/2026]. See the Terms and Conditions (https://onlinelibrary.wiley.com/terms-and-conditions) on Wiley Online Library for rules of use; OA articles are governed by the applicable Creative Commons License

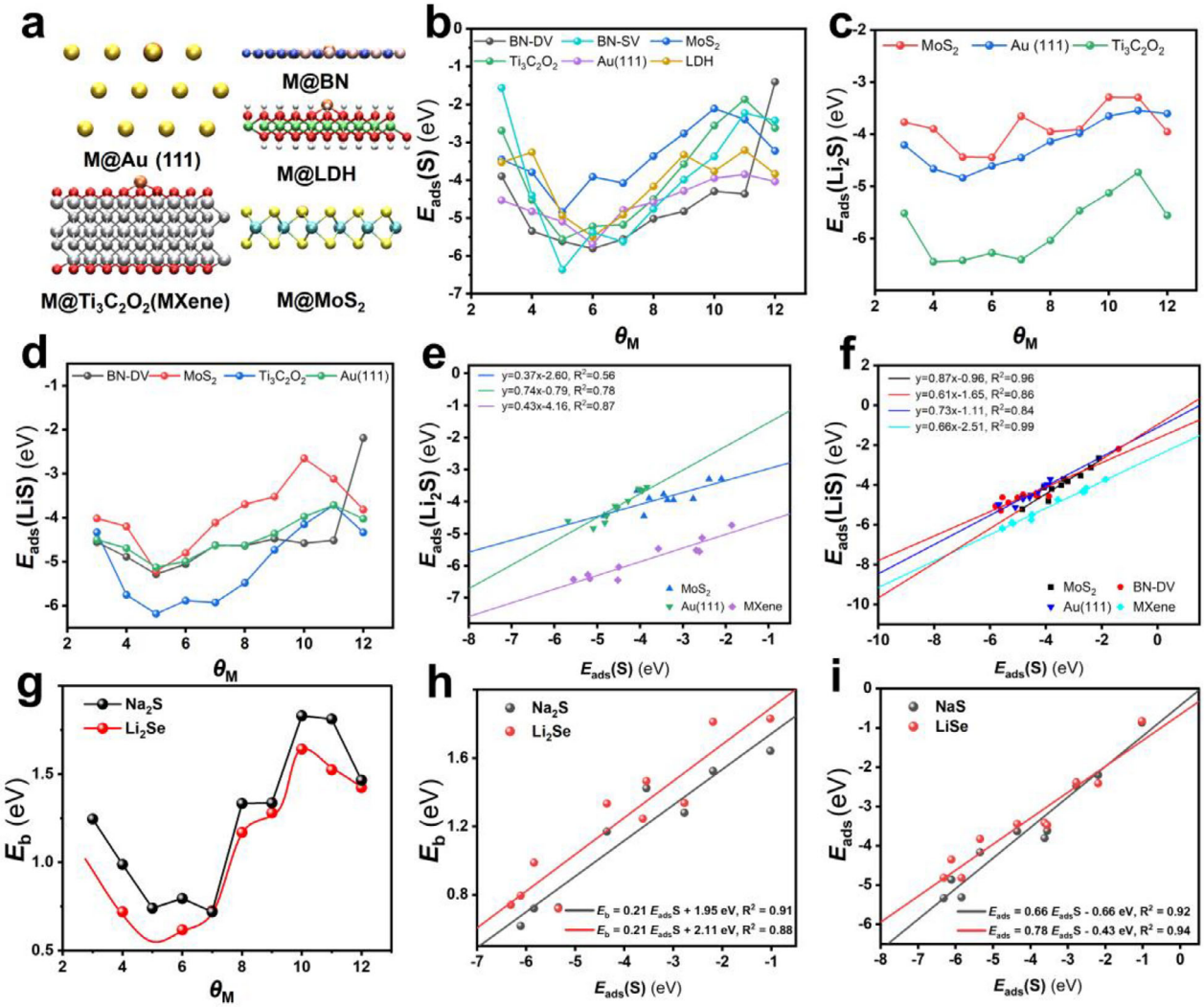


FIGURE 8 | Extension of U-type rules and E_{ads}(S) descriptor to other 2D SACs and metal–chalcogenide batteries. (a) Side view of 4*d* TMs anchored by BN, MoS_2, LDH (NiOOH), Au (111), and $Ti_3C_2O_2$ (MXene), in which H, B, C, N, O, S, Ti, Ni, Mo, and Au elements are white, pink, silver, blue, red, yellow, gray, green, cyan, and gold, respectively. (b–d) Dependence of E_{ads}(S) (b), E_{ads}(Li_2S) (c), and E_{ads}(LiS) (d) on valence electrons of 4*d* TMs. (e–f) Linear correlation of E_{ads}(Li_2S) (e) and E_{ads}(LiS) (f) with E_{ads}(S). (g) E_b values of Na_2S/Li_2Se decomposition as a function of valence electrons of 4*d* TMs in MN_4 SACs. (h) Linear correlation of E_{ads}(S) and E_b values of Na_2S and Li_2Se decompositions. (i) Linear correlation of E_{ads}(LiSe/NaS) with E_{ads}(S).

U-type trends (Figure 8g). Furthermore, these E_b values show excellent linear correlations with the E_{ads}(S) (Figure 8h). Notably, the primary difference of fitted lines (Figures 6f and 8h) across Li–S, Na–S, and Li–Se systems lies in the intercept values (2.23, 1.95, and 2.11, respectively), indicating that E_{ads}(S) can predict efficiently the E_b values of decompositions of Li_2S, Na_2S, and Li_2Se. That is to say that E_{ads}(S) is an efficient descriptor for predicting the kinetics of oxidation of S/Se in alkali–metal-sulfur/selenium batteries.

For the discharge process, the adsorption energy of LiSe/NaS is the key to determine the reaction kinetics as evaluated by the overpotential. A strong linear interrelations of adsorption energy of NaS/LiSe with E_{ads}(S) (R^2 of 0.94/0.92) was identified (Figure 8i), revealing that the adsorption energy of S atom can serve as an effective descriptor for predicting the performance of SACs for S/Se reduction reaction in metal-sulfur/selenium batteries. Nevertheless, due to the volcanic relationship between E_{ads}(NaS/LiSe) and corresponding overpotential, coordination engineering of SACs is still essential for obtaining optimal adsorption strength and thus the competitive overpotential of the reduction reaction of S/Se in M–S and M–Se batteries.

Overall, combined with *Q*-AIM, E_{ads}(S) exhibits transferable performance in predicting the catalytic performance of SACs supported by various 2D SACs (Graphene, C_3N, MoS_2, MXene, and Au (111)) for charge–discharge in LSB, even in metal-sulfur/selenium batteries. Based on limited data, we demonstrated that our proposed descriptor enriches and demonstrates the correlation of species adsorption and catalytic performance upon diverse SACs and energy-storage devices, moving beyond semi-empirical correlations [45]. These findings underscore the necessity for deeper investigations and provide new perspec-

15214095, 0, Downloaded from https://advanced.onlinelibrary.wiley.com/doi/10.1002/adma.74445 by Wei Lin - Zhongshan University , Wiley Online Library on [04/08/2026]. See the Terms and Conditions (https://onlinelibrary.wiley.com/terms-and-conditions) on Wiley Online Library for rules of use; OA articles are governed by the applicable Creative Commons License

tives for designing SACs for various alkali–metal chalcogenide batteries.

3 | Conclusion

In conclusion, metal-support interaction in covalently coordinated SACs plays a key role in determining the species adsorption as well as the catalytic performance. We proposed *Q*-AIM describing the interaction strength between adsorbates (single atom of C, N, O and S) and active sites that are covalently bonded to their neighboring atoms. This model captures the formation of a metal-centered quasi-atomic entity with *spd*-hybridized valence shells, which exhibits a preference for full occupation with up to 18 electrons. Orbital-wise interaction analysis reveals that the progressive occupation of antibonding states destabilizes adsorption, allowing *Q*-AIM to accurately explain the physical origins of the single extremum of adsorption energy of a single S atom (E_{ads}(S)) across covalent SACs. This work represents a significant advance over prior theory [23], which successfully located a single adsorption energy extremum for free-atom-like 4*d*/5*d* dopants in SAAs based on the 10-electron rule, but was unable to identify a similar extremum for covalently bonded TMs on different supports. Additional DFT calculations show that E_{ads}(S) can serve as a descriptor for predicting SRR/SER performance, which can be extended to rational design of SACs suitable for metal-sulfur/selenium batteries. Using our newly identified electron-counting rule and E_{ads}(S) as input and output, respectively, we trained the CatBoost machine learning model, which confirmed the 18-electron rule and screened a series of high-performance SACs—previously rarely reported—from a pool of ~800,000 candidates. For SER, the SACs with metal centers of Nb, Mo, Hf, Ta, W, and Re exhibit superior catalytic performance. In case of SRR, more than 8000 SACs have been screened out due to their optimal adsorption strength to S atoms. This study demonstrates a seamless integration from model development to practical application, enabled by a combined DFT and machine learning methodology, and opens new avenues for designing SACs toward a broader range of electrochemical reactions in the future.

Author Contributions

Chenhui Wang and **Wei Lin** contributed equally. All authors have given approval to the final version of the manuscript.

Acknowledgements

This work was financially supported by the National Natural Science Foundation of China (Grants nos. 52372254 and 52432007) and Special Funds for the Cultivation of Guangdong College Students' Scientific and Technological Innovation (Grants nos. pdjh2024a003 and pdjh2025bc006).

Conflicts of Interest

The authors declare no conflicts of interest.

Data Availability Statement

The data that support the findings of this study are available from the corresponding author upon reasonable request.

References

1. X. Wang, Y. Zhang, J. Wu, et al., "Single-Atom Engineering to Ignite 2D Transition Metal Dichalcogenide Based Catalysis: Fundamentals, Progress, and Beyond," *Chemical Reviews* 122 (2021): 1273–1348, https://doi.org/10.1021/acs.chemrev.1c00505.

2. J. George, S. Thangarasu, A. Jayaram, and J. J. Periyanayagam, "Materials for Electrocatalysis: Future Prospects in Energy Conversion," *Chemical Record* 25 (2025): 202400254, https://doi.org/10.1002/tcr.202400254.

3. X. Wu, R. Xie, D. Cai, et al., "Engineering Defect-Rich Bimetallic Telluride With Dense Heterointerfaces for High-Performance Lithium–Sulfur Batteries," *Advanced Functional Materials* 34 (2024): 2315012, https://doi.org/10.1002/adfm.202315012.

4. F. Calle-Vallejo, J. I. Martinez, J. M. Garcia-Lastra, J. Rossmeisl, and M. T. Koper, "Physical and Chemical Nature of the Scaling Relations Between Adsorption Energies of Atoms on Metal Surfaces," *Physical Review Letters* 108 (2012): 116103, https://doi.org/10.1103/PhysRevLett.108.116103.

5. Z. He, J. Wang, and B. Ouyang, "Design Principle of Carbon-Supported Single-Atom Catalysts—Interplay Between *d*-Orbital Periodicity and Local Hybridization," *Chemistry of Materials* 36 (2024): 1405–1412, https://doi.org/10.1021/acs.chemmater.3c02549.

6. X. Shi, Z. Wen, Q. Gu, et al., "Metal–Support Frontier Orbital Interactions in Single-Atom Catalysis," *Nature* 640 (2025): 668–675, https://doi.org/10.1038/s41586-025-08747-z.

7. P. Zeng, X. Li, B. Zhao, et al., "Electronic Structure Engineering in Electrocatalysts: Enabling Regulated Redox Mediation for Advanced Lithium-Sulfur Chemistry," *Advanced Energy Materials* 15 (2025): 2501603, https://doi.org/10.1002/aenm.202501603.

8. R. Zhou, S. N. Gu, M. Guo, S. Z. Xu, and G. W. Zhou, "Progresses and Prospects of Asymmetrically Coordinated Single Atom Catalysts for Lithium–Sulfur Batteries," *Energy & Environmental Materials* 7 (2024): 12703, https://doi.org/10.1002/eem2.12703.

9. J. Koppe, A. V. Yakimov, D. Gioffrè, et al., "Coordination Environments of Pt Single-Atom Catalysts From NMR Signatures," *Nature* 642 (2025): 613–619, https://doi.org/10.1038/s41586-025-09068-x.

10. K. Cheng, X. Huang, Y. Li, et al., "Atom-Level 2D Catalysts Accelerating Deposition/Dissolution Kinetics in Lithium–Sulfur Batteries," *Advanced Functional Materials* 35 (2024): 2410742, https://doi.org/10.1002/adfm.202410742.

11. W. Yan, W. Chen, and Y. Chen, "Recent Design Strategies for M-N-C Single-Atom Catalysts in Oxygen Reduction: An Entropy Increase Perspective," *Advanced Functional Materials* 34 (2024): 2401027, https://doi.org/10.1002/adfm.202401027.

12. Y. Wang, A. Cho, G. Jia, et al., "Tuning Local Coordination Environments of Manganese Single-Atom Nanozymes With Multi-Enzyme Properties for Selective Colorimetric Biosensing," *Angewandte Chemie International Edition* 62 (2023): 202300119, https://doi.org/10.1002/anie.202300119.

13. Z. Fu, B. Yang, and R. Wu, "Understanding the Activity of Single-Atom Catalysis From Frontier Orbitals," *Physical Review Letters* 125 (2020): 156001, https://doi.org/10.1103/PhysRevLett.125.156001.

14. J. C. Liu, F. Luo, and J. Li, "Electrochemical Potential-Driven Shift of Frontier Orbitals in M–N–C Single-Atom Catalysts Leading to Inverted Adsorption Energies," *Journal of the American Chemical Society* 145 (2023): 25264–25273, https://doi.org/10.1021/jacs.3c08697.

15. X. Zhao, Y. Sun, J. Wang, et al., "Regulating *d* -Orbital Hybridization of Subgroup-IVB Single Atoms for Efficient Oxygen Reduction Reaction," *Advanced Materials* 36 (2024): 2312117, https://doi.org/10.1002/adma.202312117.

16. S. Zhang, Y. Kong, Y. Gu, et al., "Strong $d-\pi$ Orbital Coupling of Co–C_4 Atomic Sites on Graphdiyne Boosts Potassium–Sulfur Battery Electrocatalysis," *Journal of the American Chemical Society* 146 (2024): 4433–4443, https://doi.org/10.1021/jacs.3c09533.

15214095, 0, Downloaded from https://advanced.onlinelibrary.wiley.com/doi/10.1002/adma.74445 by Wei Lin - Zhongshan University , Wiley Online Library on [04/08/2026]. See the Terms and Conditions (https://onlinelibrary.wiley.com/terms-and-conditions) on Wiley Online Library for rules of use; OA articles are governed by the applicable Creative Commons License

17. G. Yu, X. Liu, W. Huang, et al., "Ferromagnetic Atomic *d-p* Orbital Hybridization for Promoting Al-S Batteries," *Advanced Materials* 37 (2025): 2418784, https://doi.org/10.1002/adma.202418784.

18. G. Wu, T. Liu, Z. Lao, et al., "Optimizing s–p Orbital Overlap Between Sodium Polysulfides and Single-Atom Indium Catalyst for Efficient Sulfur Redox Reaction," *Angewandte Chemie International Edition* 64 (2025): 202422208, https://doi.org/10.1002/anie.202422208.

19. W. Wang, J. Si, L. Yue, et al., "Bimetallic Active Sites With Tailored *d*-Bands Boost Multistep Sulfur Redox Reactions for Enhanced Lithium-Sulfur Battery Performance," *Chemical Engineering Journal* 507 (2025): 160363, https://doi.org/10.1016/j.cej.2025.160363.

20. J. Pu, Y. Tan, J. Yin, et al., "Promoting Effect of *d*-Band Center and In-Situ Precipitation Strategy on Sulfur Evolution Reaction," *Journal of Energy Chemistry* 104 (2025): 740–748, https://doi.org/10.1016/j.jechem.2025.01.030.

21. Z. Shen, X. Jin, J. Tian, et al., "Cation-Doped ZnS Catalysts for Polysulfide Conversion in Lithium–Sulfur Batteries," *Nature Catalysis* 5 (2022): 555–563, https://doi.org/10.1038/s41929-022-00804-4.

22. Z. Shang, S. Zhao, Q. Dang, F. Wang, X. Sun, and H. Li, "A General Machine-Learning Framework for High-Throughput Screening for Stable and Efficient RuO_2-Based Acidic Oxygen Evolution Reaction Catalysts," *ACS Catalysis* 15 (2025): 12835–12847, https://doi.org/10.1021/acscatal.5c02247.

23. J. Schumann, M. Stamatakis, A. Michaelides, and R. Reocreux, "Ten-Electron Count Rule for the Binding of Adsorbates on Single-Atom Alloy Catalysts," *Nature Chemistry* 16 (2024): 749–754, https://doi.org/10.1038/s41557-023-01424-6.

24. M. T. Greiner, T. E. Jones, S. Beeg, et al., "Free-Atom-Like *d* States in Single-Atom Alloy Catalysts," *Nature Chemistry* 10 (2018): 1008–1015, https://doi.org/10.1038/s41557-018-0125-5.

25. L. Peng, Z. Wei, C. Wan, et al., "A Fundamental Look at Electrocatalytic Sulfur Reduction Reaction," *Nature Catalysis* 3 (2020): 762–770, https://doi.org/10.1038/s41929-020-0498-x.

26. H. Ma, X. Ye, X. Li, Z. J. Xu, and Y. Sun, "Ferroelectric Polarization Effects of Single-Atom Catalysts on Water Oxidation," *Advanced Materials* 37 (2025): 2500285, https://doi.org/10.1002/adma.202500285.

27. L. Liu, T. Liu, C. Xu, et al., "Fecocumnrub Nanobox with Dual Driving of High-Entropy and Electron-Trap Effects as the Efficient Electrocatalyst for Water Oxidation," *Nano Letters* 24 (2024): 2831–2838, https://doi.org/10.1021/acs.nanolett.3c04962.

28. H. Park, H. S. Koh, and D. J. Siegel, "First-Principles Study of Redox End Members in Lithium–Sulfur Batteries," *Journal of Physical Chemistry C* 119 (2015): 4675–4683, https://doi.org/10.1021/jp513023v.

29. L. Ren, K. Sun, Y. Wang, et al., "Tandem Catalysis Inside Double-Shelled Nanocages with Separated and Tunable Atomic Catalyst Sites for High Performance Lithium-Sulfur Batteries," *Advanced Materials* 36 (2023): 2310547, https://doi.org/10.1002/adma.202310547.

30. S. Wu, C. Wang, H. Liang, et al., "High-Throughput Calculations for Screening *d* - and *p* -Block Single-Atom Catalysts Toward Li_2S/Na_2S Decomposition Guided by Facile Descriptor Beyond Brønsted–Evans–Polanyi Relationship," *Small* 20 (2024): 2305161, https://doi.org/10.1002/smll.202305161.

31. Z. Lian, M. Yang, F. Jan, and B. Li, "Machine Learning Derived Blueprint for Rational Design of the Effective Single-Atom Cathode Catalyst of the Lithium–Sulfur Battery," *Journal of Physical Chemistry Letters* 12 (2021): 7053–7059, https://doi.org/10.1021/acs.jpclett.1c00927.

32. Z. Zeng, W. Nong, Y. Li, and C. Wang, "Universal-Descriptors-Guided Design of Single Atom Catalysts Toward Oxidation of Li_2S in Lithium–Sulfur Batteries," *Advanced Science* 8 (2021): 2102809, https://doi.org/10.1002/advs.202102809.

33. H. Xu, D. Cheng, D. Cao, and X. C. Zeng, "Revisiting the Universal Principle for the Rational Design of Single-Atom Electrocatalysts," *Nature Catalysis* 7 (2024): 207–218, https://doi.org/10.1038/s41929-023-01106-z.

34. H. Li, R. Meng, and C. Ye, "Developing High-Power Li||S Batteries Via Transition Metal/Carbon Nanocomposite Electrocatalyst Engineering," *Nature Nanotechnology* 19 (2024): 792, https://doi.org/10.1038/s41565-024-01614-4.

35. P. Xu, J. Han, W. Chen, J. C. Ren, S. Li, and H. Xia, "An Effective Single-Atom Catalytic Descriptor for Accelerating Sulfur Reduction Reaction in Lithium-Sulfur Batteries," *Advanced Materials* (2025): 15380, https://doi.org/10.1002/adma.202515380.

36. T. Bligaard, J. K. Nørskov, S. Dahl, J. Matthiesen, C. H. Christensen, and J. Sehested, "The Brønsted–Evans–Polanyi Relation and the Volcano Curve in Heterogeneous Catalysis," *Journal of Catalysis* 224 (2004): 206–217, https://doi.org/10.1016/j.jcat.2004.02.034.

37. A. Michaelides, Z. P. Liu, C. J. Zhang, A. Alavi, D. A. King, and P. Hu, "Identification of General Linear Relationships Between Activation Energies and Enthalpy Changes for Dissociation Reactions at Surfaces," *Journal of the American Chemical Society* 125 (2003): 3704–3705, https://doi.org/10.1021/ja027366r.

38. R. A. van Santen, M. Neurock, and S. G. Shetty, "Reactivity Theory of Transition-Metal Surfaces: A Brønsted−Evans−Polanyi Linear Activation Energy−Free-Energy Analysis," *Chemical Reviews* 110, no. 2005 (2010): 2005–2048, https://doi.org/10.1021/cr9001808.

39. S. C. Rasmussen, "The 18-Electron Rule and Electron Counting in Transition Metal Compounds: Theory and Application," *ChemTexts* 1 (2015): 10, https://doi.org/10.1007/s40828-015-0010-4.

40. A. Kraskov, H. Stogbauer, and P. Grassberger, "Estimating Mutual Information," *Physical Review E* 69 (2004): 066138, https://doi.org/10.1103/PhysRevE.69.066138.

41. B. C. Ross, "Mutual Information Between Discrete and Continuous Data Sets," *PLoS ONE* 9 (2014): 87357, https://doi.org/10.1371/journal.pone.0087357.

42. S. Chatterjee, "A New Coefficient of Correlation," *Journal of the American Statistical Association* 116 (2009): 2009–2022, https://doi.org/10.1080/01621459.2020.1758115.

43. L. Prokhorenkova, G. Gusev, A. Vorobev, A. V. Dorogush, and A. Gulin, "CatBoost: Unbiased Boosting With Categorical Features," in *Advances in Neural Information Processing Systems* 31 (2018): 6639.

44. S. M. Lundberg and S.-I. Lee, "A Unified Approach to Interpreting Model Predictions," in *Proceedings of the 31st International Conference on Neural Information Processing Systems NIPS* (2017): 4768.

45. X. Han, Z. Zhang, and X. Xu, "Single Atom Catalysts Supported on N-Doped Graphene Toward Fast Kinetics in Li–S Batteries: A Theoretical Study," *Journal of Materials Chemistry A* 9 (2021): 12225–12235, https://doi.org/10.1039/d1ta01948a.

Supporting Information

Additional supporting information can be found online in the Supporting Information section.

Supporting File: adma74445-sup-0001-SuppMat.pdf.

15214095, 0, Downloaded from https://advanced.onlinelibrary.wiley.com/doi/10.1002/adma.74445 by Wei Lin - Zhongshan University , Wiley Online Library on [04/08/2026]. See the Terms and Conditions (https://onlinelibrary.wiley.com/terms-and-conditions) on Wiley Online Library for rules of use; OA articles are governed by the applicable Creative Commons License